Figure 1.

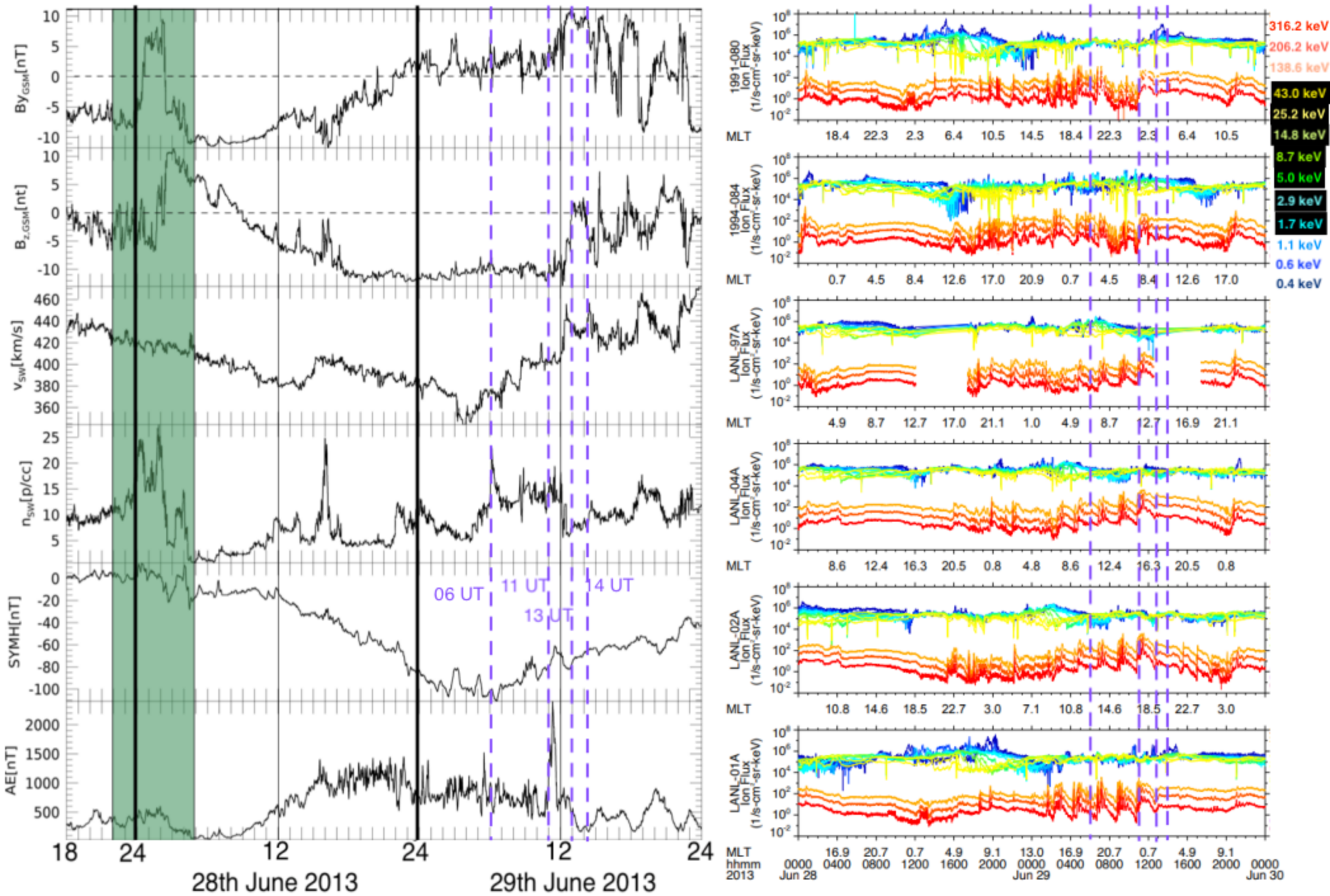
By_GSM[nT]
B_z,GSM[nt]
v_SW[km/s]
n_SW[p/cc]
SYMH[nT]
AE[nT]
06 UT
11 UT
13 UT
14 UT
18
24
12
24
12
24
28th June 2013
29th June 2013
1991-080 Ion Flux (1/s-cm²-sr-keV)
1994-084 Ion Flux (1/s-cm²-sr-keV)
LANL-97A Ion Flux (1/s-cm²-sr-keV)
LANL-04A Ion Flux (1/s-cm²-sr-keV)
LANL-02A Ion Flux (1/s-cm²-sr-keV)
LANL-01A Ion Flux (1/s-cm²-sr-keV)
316.2 keV
206.2 keV
138.6 keV
43.0 keV
25.2 keV
14.8 keV
8.7 keV
5.0 keV
2.9 keV
1.7 keV
1.1 keV
0.6 keV
0.4 keV
MLT
hhmm 2013
0000 Jun 28
0400
0800
1200
1600
2000
0000 Jun 29
0400
0800
1200
1600
2000
0000 Jun 30

Figure 2.

UT on 29th June 2013

a) Ion Pressure

b) Ion Pressure Anisotropy

c) Ion Energy Spectrum at Pressure Peak

CIMI | TWINS | CIMI | TWINS | CIMI | TWINS

06:00 UT
IMF Bz < 0
AE ~ 1000 nT

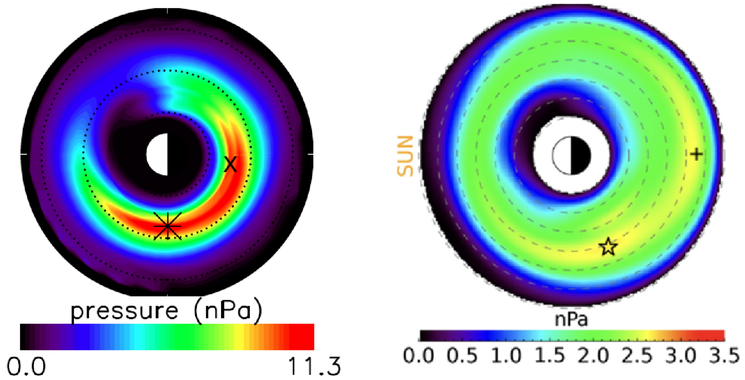

11:00 UT
IMF Bz < 0
AE ~ 2500 nT

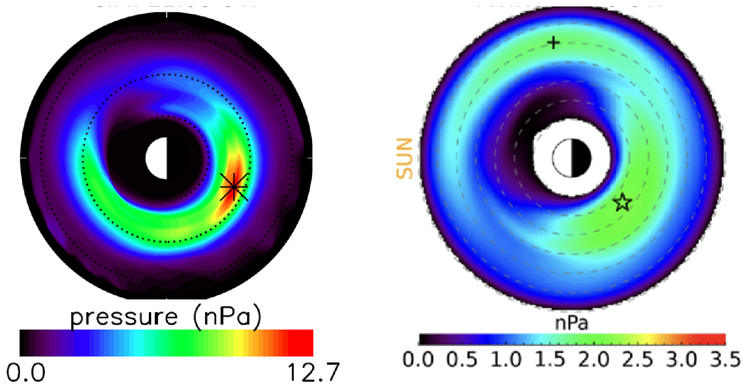

13:00 UT
IMF Bz > 0
AE ~ 600 nT
IMF By ~11 nT

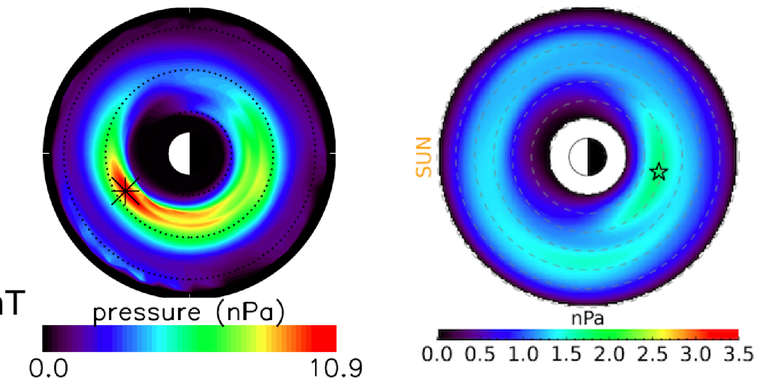

14:00 UT
IMF Bz > 0
AE ~ 200 nT
IMF By ~10 nT

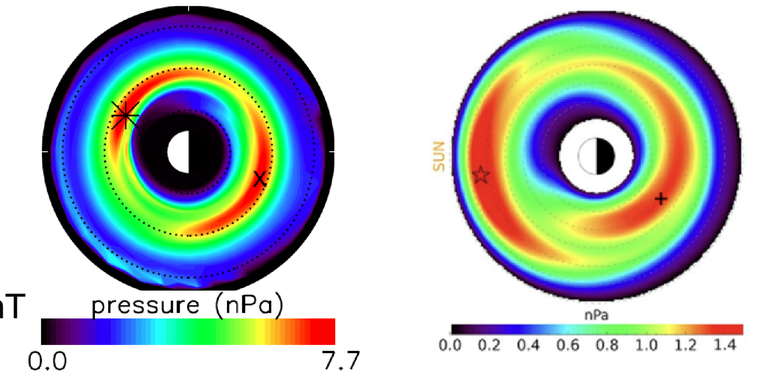

Figure 3.

a) Ion Intensity

b) Ion Energy at spectral peak

UT on 29th June 2013

CIMI

TWINS

CIMI

TWINS

06:00 UT
IMF Bz < 0
AE ~ 1000 nT

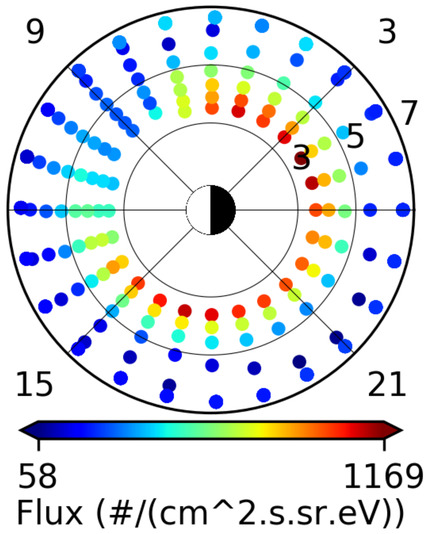

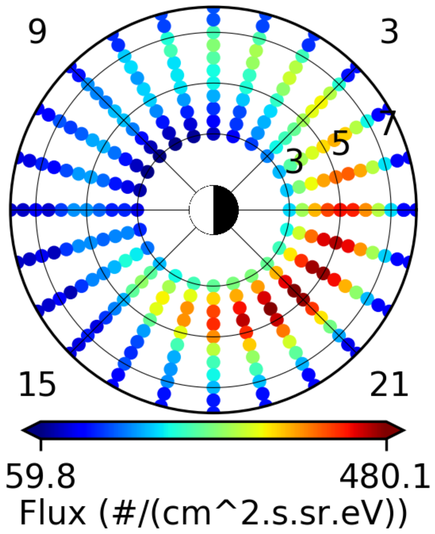

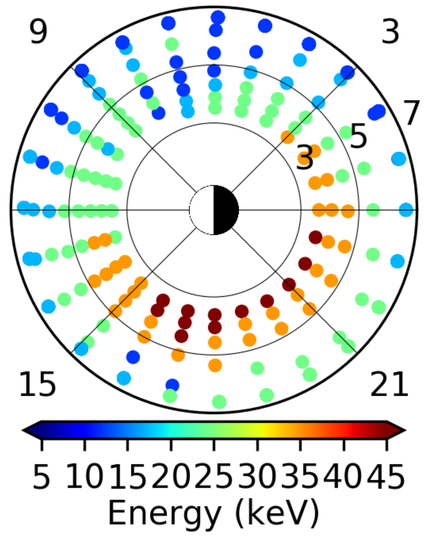

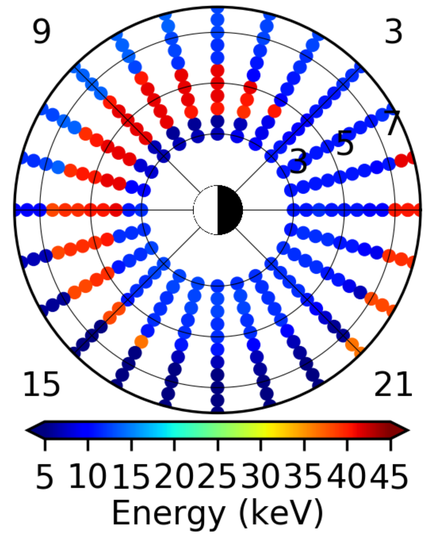

11:00 UT
IMF Bz < 0
AE ~ 2500 nT

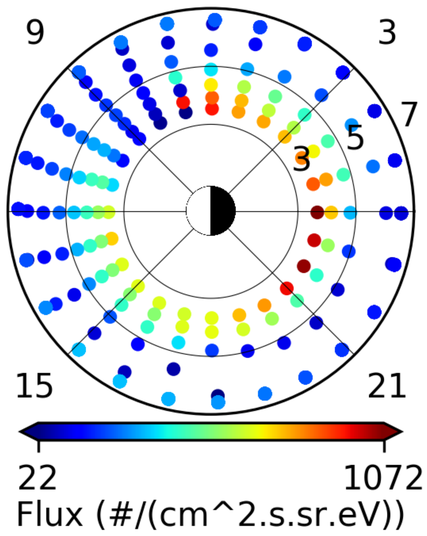

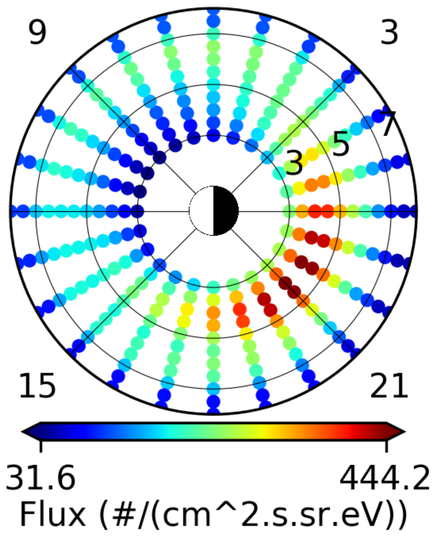

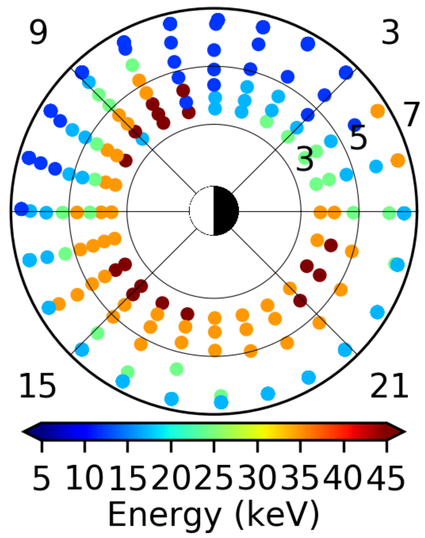

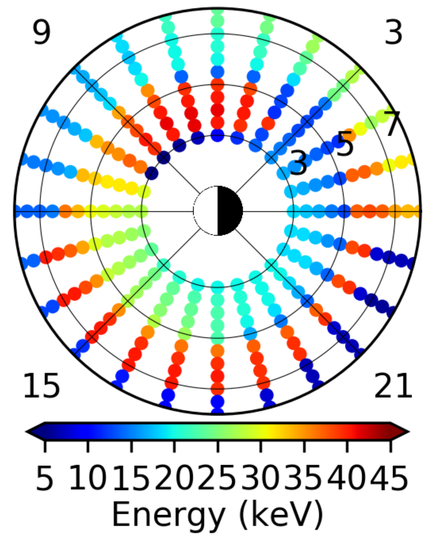

13:00 UT
IMF Bz > 0
AE ~ 600 nT
IMF By ~11 nT

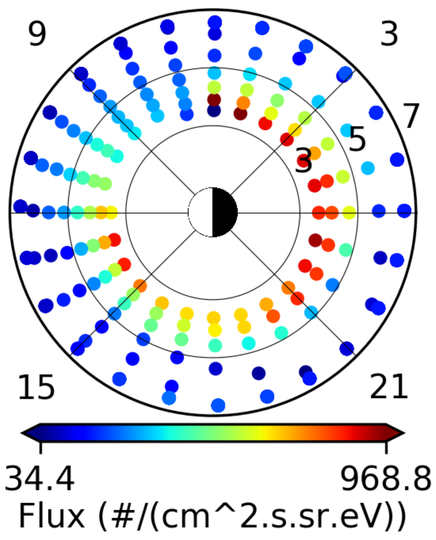

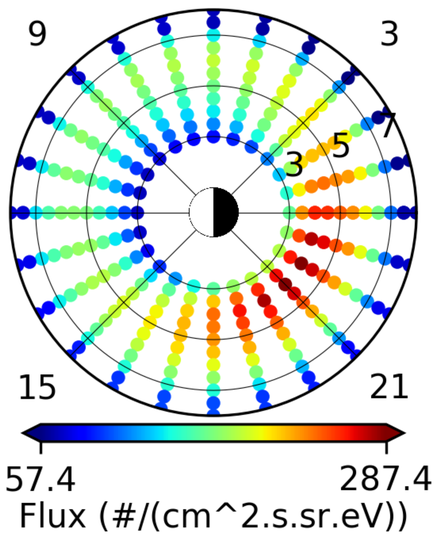

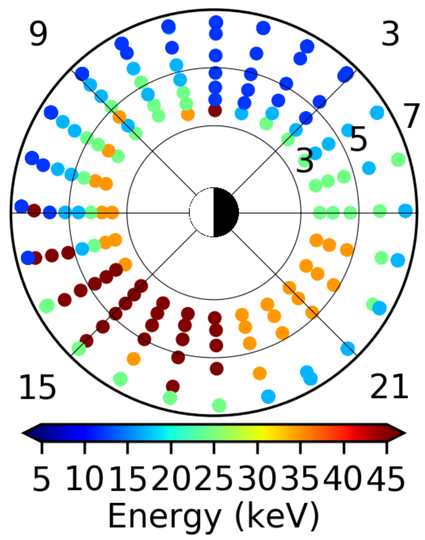

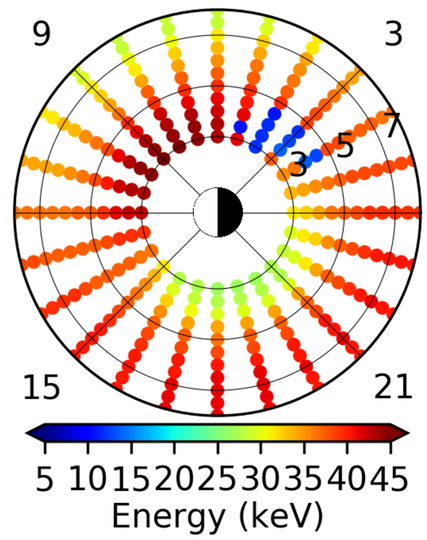

14:00 UT
IMF Bz > 0
AE ~ 200 nT
IMF By ~10 nT

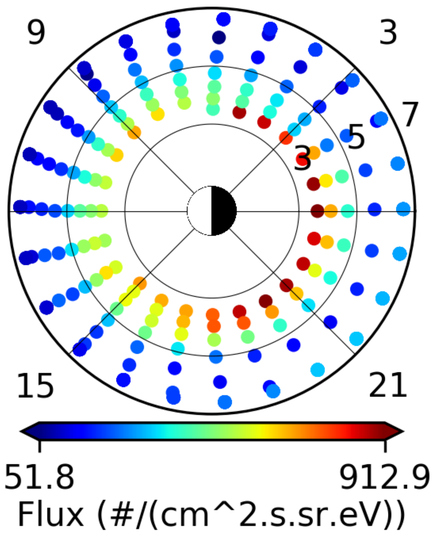

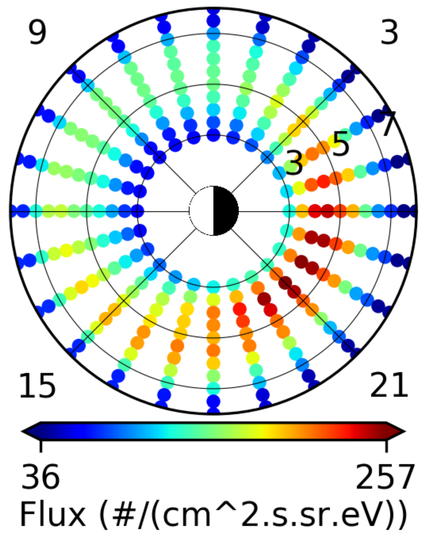

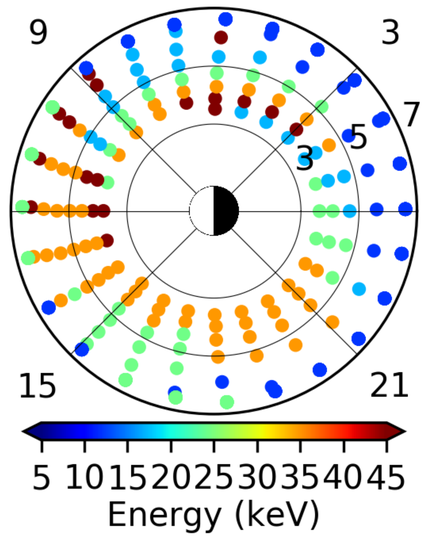

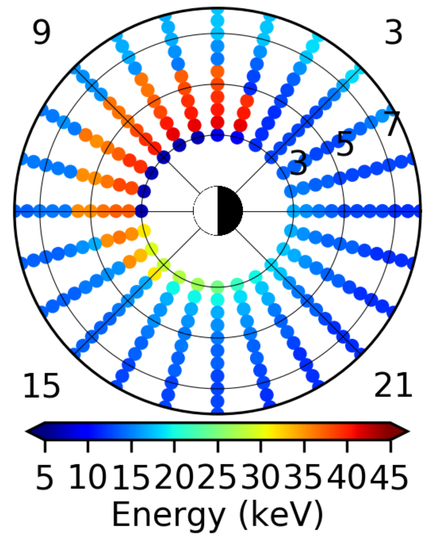

Figure 4.

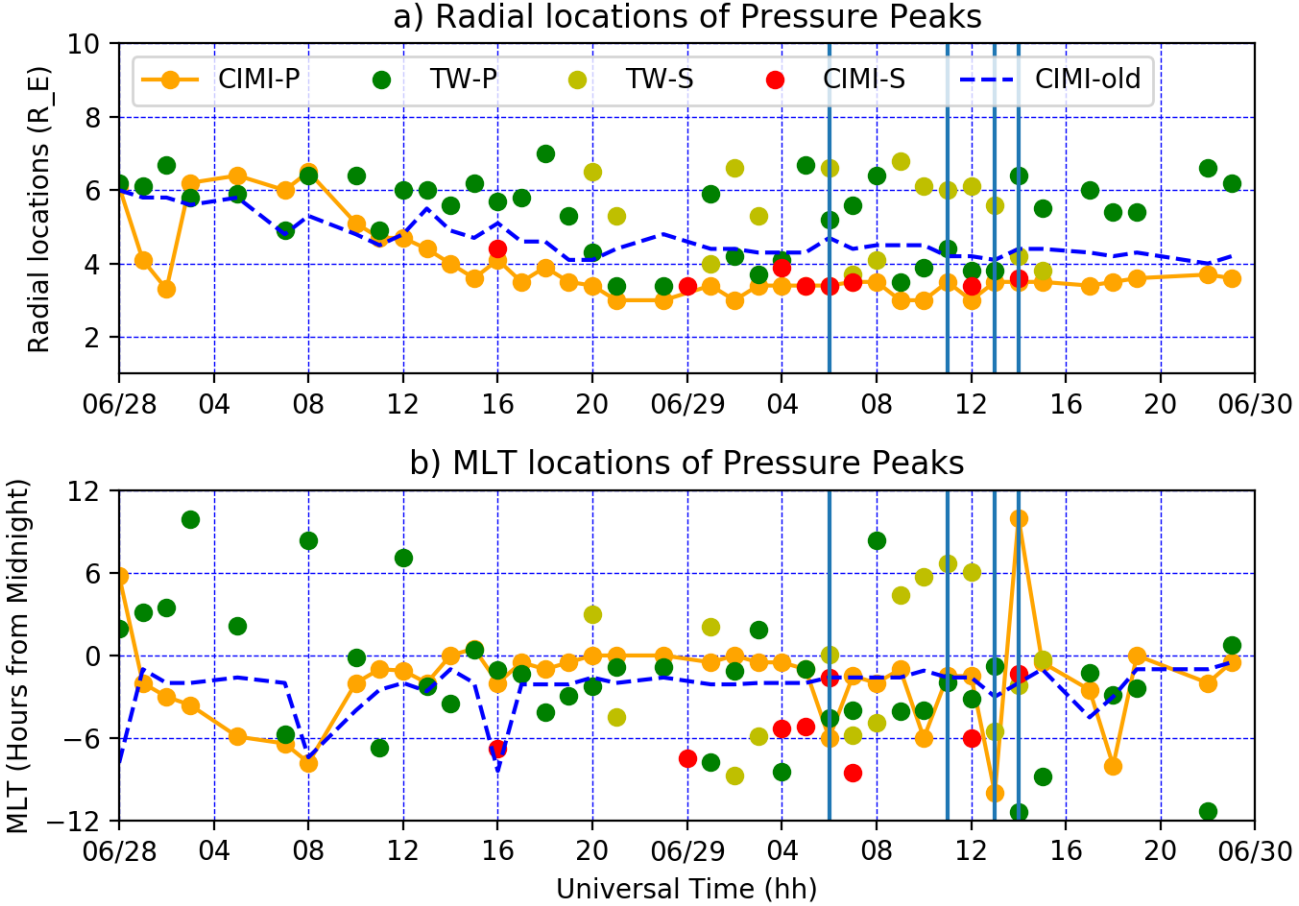
a) Radial locations of Pressure Peaks
CIMI-P
TW-P
TW-S
CIMI-S
CIMI-old
Radial locations (R_E)
10
8
6
4
2
06/28
04
08
12
16
20
06/29
04
08
12
16
20
06/30
b) MLT locations of Pressure Peaks
MLT (Hours from Midnight)
12
6
0
−6
−12
06/28
04
08
12
16
20
06/29
04
08
12
16
20
06/30
Universal Time (hh)

Comparisons of TWINS Observations with CIMI Calculations during ion injections on 29th June 2013

S. Shekhar[3], C. Ferradas[2,5], M. C. Fok[2], J. D. Perez[1], M. Henderson[4]

[1]Department of Physics, Auburn University, AL, USA
[2]NASA Goddard Space Flight Center, Greenbelt, MD, USA
[3]Department of Physics, University of Iowa, IA, USA
[4]Los Alamos National Lab, NM, USA
[5]Department of Physics, Catholic University of America, Washington DC, USA

Key Points:

- TWINS global ring current observations and results from CIMI simulations were compared for a geomagnetic storm on 28-29 June 2013.
- In the recovery phase, CIMI produced two ion pressure peaks and electric field shielding effects in agreement with TWINS observations.
- TWINS ring current ion pressure profiles were more sensitive to AE fluctuations than CIMI simulations.

Corresponding author: Sapna Shekhar, sapna-shekhar@uiowa.edu

Abstract

In a recent study by Shekhar et. al. 2021, a moderate geomagnetic storm (sym-H∼-100 nT) during 28th-29th June 2013 was studied using CIMI (Comprehensive Inner Magnetosphere-Ionosphere) simulations and results were compared with TWINS (Two wide-angle Imaging Neutral-atom Spectrometers) observations. The CIMI simulations did not include ion injections. As a result, TWINS and CIMI results were found to disagree on the number and locations of ion pressure peaks and ion drift patterns. In this study, CIMI simulations were performed with the inclusion of ion injections using the geosynchronous particle flux data from 6 LANL satellites as boundary conditions. Comparisons of the spatial and temporal evolution of ring current (RC) ions including ion pressure, anisotropy, intensity and median energy, the ion spectrum at the ion pressure peak locations show improved agreements with TWINS observations, specifically in the recovery phase post 06 UT on 29th June, when rapid AE index fluctuations were observed.

Plain Language Summary

The Sun emits solar wind particles that enter the inner magnetosphere mostly from the nightside due to the interactions with Earth's magnetic fields. These charged particles drift azimuthally around the Earth, in directions dependent on the charge of the particle, hence driving a net current around the Earth, called ring currents (RC). In this study, the spatial and temporal evolution of RC during a geomagnetic storm between 28-29 June 2013 are explored through a comparison of results from a physics based model (CIMI) with observed imager data from TWINS. The CIMI model also includes ion flux data from 6 LANL satellites to account for incoming ions from the simulation boundary (∼ 6.6 R_E) around the Earth, which were not included in the simulations performed by Shekhar et. al. 2021 for the same time period. The various spatial and temporal RC profiles compared in this study show an improved agreement with TWINS observations relative to Shekhar et al. 2021.

1 Introduction

Ring currents (RC) are a system of large scale currents formed by the longitudinal drift motion of the trapped electrons and ions injected from the magnetotail into Earth's inner magnetosphere. Electrons and ions with energies less than 100 keV are significant constituents of RC though particle pressure is mostly contributed by ions. The convection electric field transports these particles from the plasmasheet to the magnetosphere. The radial current density at the ionosphere can be determined from the equatorial pressure (Heinemann, 1990) and hence the azimuthal shifts in the ion pressure peaks represent the variations in the Birkeland region 2 currents which are field aligned currents coupling the magnetosphere to the ionosphere.

The first direct comparisons between CIMI (using self consistent RCM electric field and Weimer2k empirical model) and TWINS ion pressure and anisotropy were made by Perez et al. (2018) for a 4-day period, 7-10 September 2015. They found that there were cases in which TWINS equatorial ion pressure showed multiple peaks that were not seen in the simulations, occuring mostly during periods of intense AE index, suggesting time and spatially dependent injections from the plasma sheet. A similar comparison was made by Shekhar et al. (2021) for a moderate geomagnetic storm (SymH∼-100 nT) for a 2-day period, 28-29 June 2013. The distribution of the incoming particles injected into the inner magnetosphere along the outer boundary of the CIMI simulation (∼$10R_E$) was taken to be isotropic, Maxwellian and uniform over local time with density and temperature (Fok et al., 2003) at any given time determined by a linear relationship to the solar wind density and velocity with a time delay of 2 hours for the solar wind effects to reach the inner plasmasheet from location of subsolar point, where the solar wind parameters were obtained. Since it was assumed to be uniform over local time, it could not capture ef-

fects due to substorm ion injections which were observed during the recovery phase of the storm starting from 06 UT on 29th June.

In this study, we have re-examined the 28-29 June 2013 storm with comparisons between TWINS observations and CIMI simulations using geosynchronous ion flux data from 6 LANL satellites at $6.6R_E$ to account for incoming particles injected into the inner magnetosphere in the simulation. Certain times during the recovery phase of the storm have been studied in detail.

2 TWINS ENA (Enegetic Neutral-atoms) Images Analysis

NASA TWINS Mission (Two wide–angle Imaging Neutral-atom Spectrometers), a pair of identical spacecrafts in two widely separated Molniya orbits with inclinations of 63.4^o, perigee altitudes of ∼1000 km, and apogees in the Northern Hemisphere at ∼7.2 RE, were launched in 2008 and enable 3–dimensional visualization of the RC dynamics. Each spacecraft is 3-axis stabilized and approximately nadir pointing and provide nearly continuous coverage of magnetospheric ENA emissions, over a broad energy range (1–100 keV/amu) with high angular ($4^o \times 4^o$) and temporal (about 1–minute) resolution.

Each TWINS instrument has sensor heads that are mounted together on a rotating actuator, which sweeps back and forth, scanning 180^o in 1 minute and then taking 22 seconds to orient in the opposite direction roughly over an Earth–centered viewing cone, scanning 180^o in another 1 minute (Goldstein & McComas, 2013) to construct a full image (Detailed description of TWINS instruments is given in McComas et al. (2009)). The images are integrated over 15–16 sweeps which implies that data is integrated over 15 minutes over a 20 minutes time period. Images are enhanced through statistical smoothening and background suppression algorithms (McComas et al., 2012). TWINS measures the time of flight of ENA thus from the velocity, the energy/amu can be derived, in the following we will refer simply to energy. ENA images are centered at ion energies ($E_{central}$) from 5 to 65 keV in 5 keV steps (i.e.13 images). The lower and upper energy range of each data point at a given central energy is given by $[\frac{E_{central}}{2}, \frac{3E_{central}}{2}]$, thus the energy ranges partially overlap to each other.

From the ENA images at 13 different energies any spatial point, equatorial distributions of ion pressure, anisotropy, pitch angle distributions and ion spectra can be obtained using a deconvolution and singular value decomposition method (Details of the method are given in Appendix A and B of Perez et al. (2012)).

3 The CIMI Model

The CIMI model is a combination of bounce-averaged kinetic model of the ring current known as Comprehensive Ring Current Model (CRCM) (Fok et al., 2001) and radiation belt environment (RBE) model (Fok et al., 2008). It takes into account charge exchange loss, energy and pitch-angle diffusion due to Whistler mode chorus waves and plasmaspheric hiss (Details of the model are available in (Fok et al., 2014)).

In this study, Fok kinetic model solves the bounce averaged Boltzmann equation with a self consistent Rice Convection model (RCM) (Harel et al., 1981) electric field. The Hardy model (Hardy et al., 1987) provides auroral conductance which is used to for the RCM calculation of the electric field. The convection potential calculation includes the modifications to the ionosphere conductance due to electron precipitation. The RC is assumed to be comprised of H^+ ions.

The distribution of the incoming particles injected into the inner magnetosphere along the outer boundary of the simulation (∼$6.6R_E$) is taken from the geosynchronous ion fluxes from the 6 LANL satellites available for the duration of the simulation (Shown in right column of Figure 1).

4 Solar Wind Conditions

The 6 panels in the left column of Figure 1 show IMF By, IMF Bz, solar wind speed, density, sym-H and AE indices (from top to bottom) respectively. The highlighted green box shows that solar wind density (n_{SW}) and IMF By have a large peak followed by rapid northward rise in IMF Bz which gradually turns southward while the solar wind speed (v_{SW}) is nearly constant. This indicates that the geomagnetic disturbance were likely initiated by corotation interaction regions (CIR). The 2 day period can be divided into 3 sections: 1) Main phase, 2) Recovery phase I and 3) Recovery phase II, where the solar wind conditions fluctuated slowly within a section but rapidly from one section to another.

The time period between 12:00 UT on 28th June to 06:00 UT on 29th June was the main phase of the storm. In this time, IMF By slowly changed direction from negative to positive, IMF Bz gradually turned southward. This indicates enhanced convection of ions from the plasmasheet. A sharp increase in solar wind density is observed around 04:00 UT on 28th June soon after which the AE index started showing rapid fluctuations. We will be refering to this time period as the Main phase.

The recovery phase of the storm started around 06:00 UT on 29th June. Between 06:00-12:00 UT on 29th June, IMF Bz remained constantly southward indicating continued enhanced convection and an increase in solar wind velocity and density was observed. A large peak in the AE index was observed around 11:00 UT on 29th June indicating substorm ion injections. We will be refering to this time period (06:00-12:00 UT on 29th June) as the Recovery phase I.

The recovery phase continued till the end of the day on 29th June. During the time period post 12:00 UT on 29th June, IMF Bz turned northward between 12:00-14:00 UT after being southward for ∼24 hours. A rapid increase in solar wind velocity, IMF By and a rapid drop in solar wind density was also observed between 12:00-14:00 UT. We will be refering to this time period (12:00-14:00 UT on 29th June) as the Recovery phase II.

5 Comparison of Spatial Profiles

The distributions of TWINS ion pressure, anisotropy, ion intensity and peak ion spectra energy were compared with CIMI simulations during the Recovery phase I and II of the geomagnetic storm. Ion pressure and anisotropy were calculated using Equations 1 and 2 in Shekhar et al. (2021). The energy range for calculations were 2.5-97.5 keV for TWINS observations and 1-121 keV for CIMI simulations. The largest ion pressure is referred to as the primary peak and the second largest distinguishable peak is referred to as the secondary peak. The second largest peak was determined through close visual inspection of the contours of ion pressure profiles. A few interesting time periods are studied in detail in this Section.

5.1 Ion Pressure, Anisotropy and Spectrum at Pressure Peak

The time evolution of spatial profiles of TWINS and CIMI ion pressure, anisotropy, and the spectrum at pressure peak are shown in Figure 2 and spatial profiles of ion intensities and energy at spectral peak are shown in Figure 3 at 06:00, 11:00, 13:00 and 14:00 UT on 29th June. In general, the CIMI distributions were found to be radially compressed relative to TWINS for all times during the storm. This is due to the fact that CIMI tends to overestimate the strength of convection at larger L shells and as a result, the penetration of particles. One possibility is that the background conductivity may be too low.

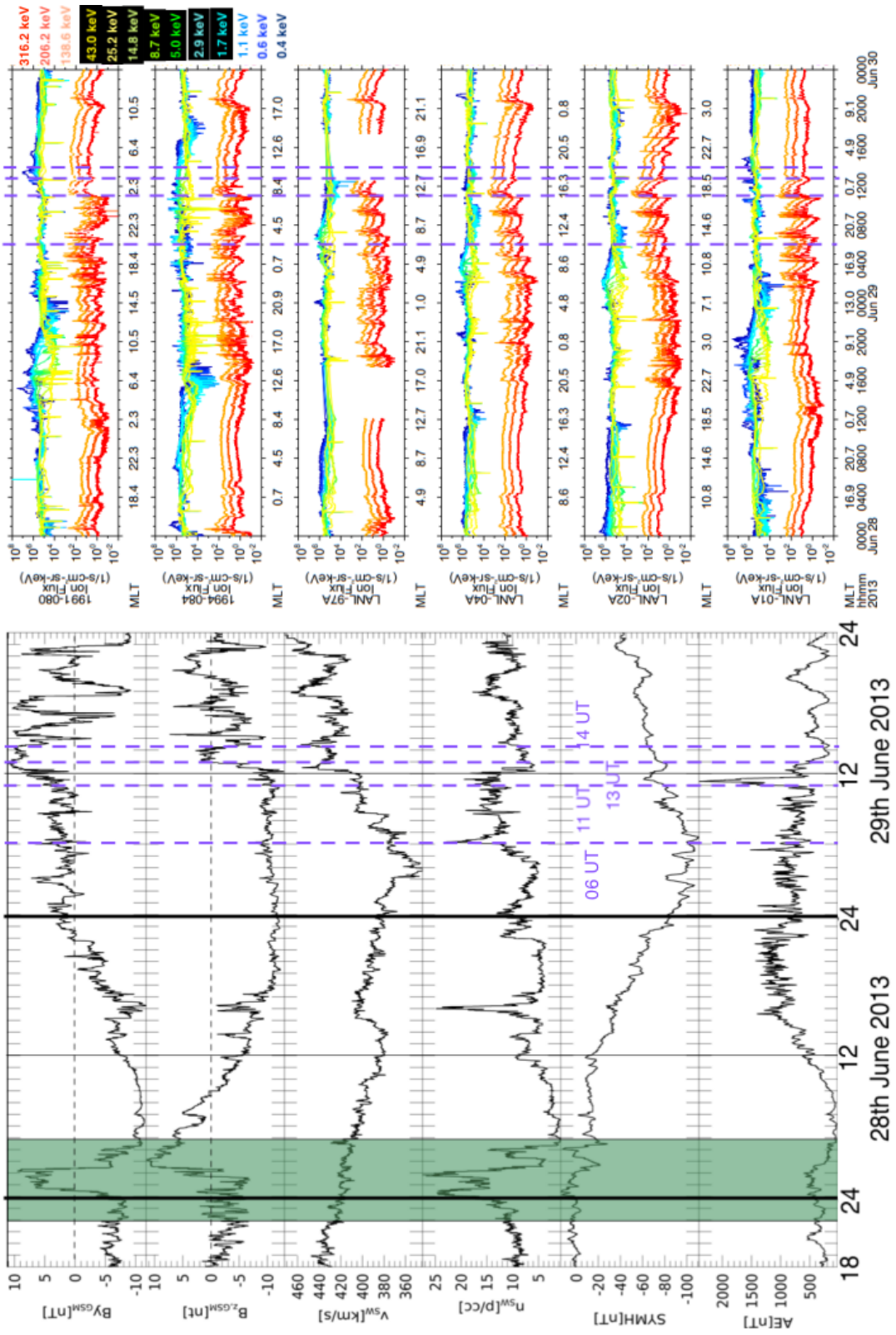

Figure 1. Solar Wind conditions for the duration of the simulation are shown on left panels with IMF By, IMF Bz, solar wind speed, density, sym-H and AE indices from top to bottom. The 6 LANL satellites available at the time are shown on the right panels. The ion fluxes were used at the outer boundary of the CIMI simulation at ~6.6 R_E. The vertical dashed lines mark the times at which detailed profiles were investigated in Section 5

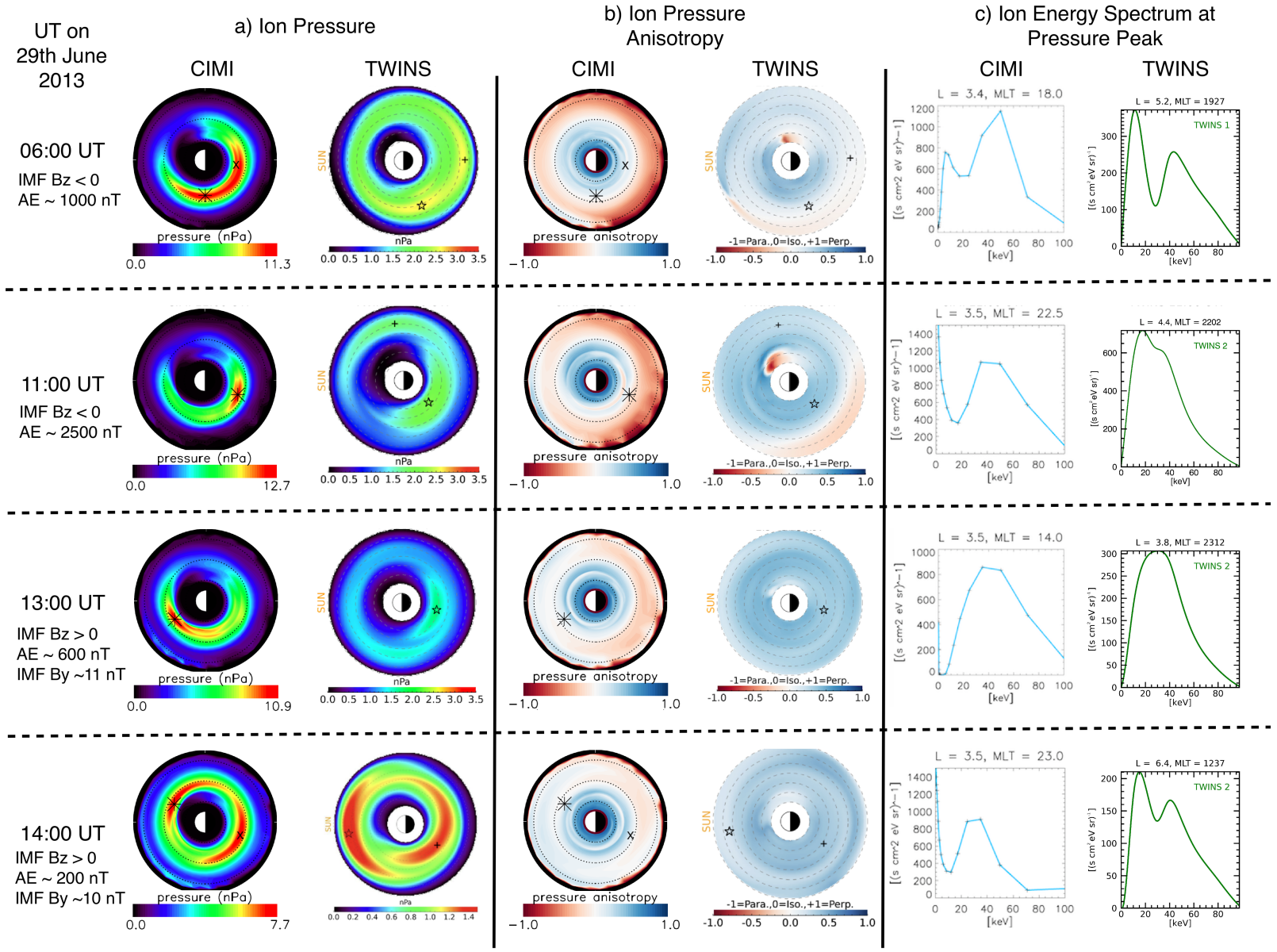

Figure 2. a. Equatorial spatial profiles of CIMI (left) and TWINS (right) ion pressures at 06:00, 11:00, 13:00 and 14:00 UT on 29th June (top to bottom). The sun is located to the left and the azimuthal coordinates represent MLT. The radial coordinates represent the radial locations mapped to SM equator. Location of maximum and second maximum ion pressure peaks are marked with black star and plus sign in TWINS respectively, and black asterik and cross sign in CIMI respectively. The concentric radial circles mark radial locations of $2R_E$, $4R_E$ and $6R_E$ in CIMI. b. Equatorial spatial profiles of CIMI (left) and TWINS (right) ion pressure anisotropies at same times as a (top to bottom). c. CIMI (left) and TWINS (right) ion energy spectrum at primary ion pressure peak locations at same times as a (top to bottom).

manuscript submitted to *Geophysical Research Letters*

Figure 1 (Left column) shows that at the start of the recovery phase I (∼06:00 UT), there had been convective transport of ions from the plasmasheet for ∼12 hours during the Main phase. The AE index had started showing rapid fluctuations from 04:00 UT indicating substorm ion injections.

Figure 2a (top) shows that CIMI and TWINS both have two distinguishable ion pressure peaks. The TWINS peaks are less than 2 hours apart in MLT and $\sim 2R_E$ apart radially, from the CIMI peaks. Around 11:00 UT, CIMI produced a single ion pressure peak approximately at similar MLT location as TWINS largest ion pressue peak but missed out TWINS secondary ion pressure peak which is observed in the morning sector at ∼7 R_E (Figure 2a, second row from top). This is likely due to the outer boundary of CIMI simulation being ∼6.6 R_E beyond which it is unlikely to capture any features. At 13:00 UT (Figure 2a, third row from top), even though CIMI produced ion pressure peak in the post noon MLT sector and TWINS observed the peak in the midnight sector, CIMI ion pressure profiles had some fine structures that are similar to TWINS but radially compressed. At 14:00 UT (Figure 2a, last row), CIMI and TWINS primary and secondary ion pressure peaks are less than 2 hours apart in MLT showing good agreement both in the number and locations of ion pressure peaks.

Figure 2b (left column) shows that a region of parallel pressure anisotropy is observed for radial distances $>5R_E$ on the midnight side for CIMI at all times. This band of parallel anisotropy on the nightside in the CIMI simulations may come from drift shell splitting. The drift shells of perpendicular ions follow the magnetic field iso-contours, so the drift shells are further away from the Earth on the dayside than on the nightside. The drift shells of parallel ions are relatively circular. Therefore, the drift shells of perpendicular ions at r $>5R_E$ on the nightside may encounter the magnetopause on the dayside, so ions are lost on the dayside. On the other hand, parallel ions drift to the dayside with similar distance inside the magnetopause and drift back to the nightside. Therefore, more parallel ions are found on the nightside at higher radial distances. Further, when the flux/pressure is low, the anisotropy could easily reach extreme values in the simulation results, leading to deviations from TWINS observed profiles.

Figure 2b shows that the time evolution of CIMI and TWINS ion anisotropies are similar. At 06 and 11 UT(Figure 2b top two rows), IMF Bz is southward and AE indices were high, a region of parallel anisotropy is observed in TWINS in the dusk to midnight sectors for radial distances >6 R_E indicating freshly injected ions. For the time periods 13 and 14 UT (Figure 2b last two rows), the AE indices were low and IMF Bz was turning northward and TWINS observed perpendicular anisotropy at all locations consistent with no substorm ion injections. CIMI also observe fewer parallel anisotropy ions at 13:00 and 14:00 UT compared to 06:00 and 11:00 UT, but as expained earlier, due to effects of drift shell splitting >5 R_E, CIMI and TWINS profiles are slightly different at larger radial locations. Figure 2c shows the CIMI and TWINS ion energy spectrum at primary ion pressure peak locations at 06:00, 11:00, 13:00 and 14:00 UT on 29th June (top to bottom). TWINS and CIMI ion spectra were mostly in agreement. TWINS median energies were found to be lower compared to CIMI.

5.2 Ion Intensity, Energy at Ion Spectral Peak

The time evolution of spatial profiles of TWINS and CIMI ion intensity and peak ion spectra energy are shown in Figure 3 at 06:00, 11:00, 13:00 and 14:00 UT on 29th June (top to bottom). The energy at spectra peak is defined as the energy at which ion energy spectra fluxes peak or median ion energy (Also defined in Shekhar et al. (2021)).

CIMI profiles were radially compressed relative to TWINS at all times but the MLT distributions were found to be similar. At 06:00 UT (Figure 3a top row), bulk of the RC ions are located between MLTs of 15 to 6 hours for both CIMI and TWINS and com-

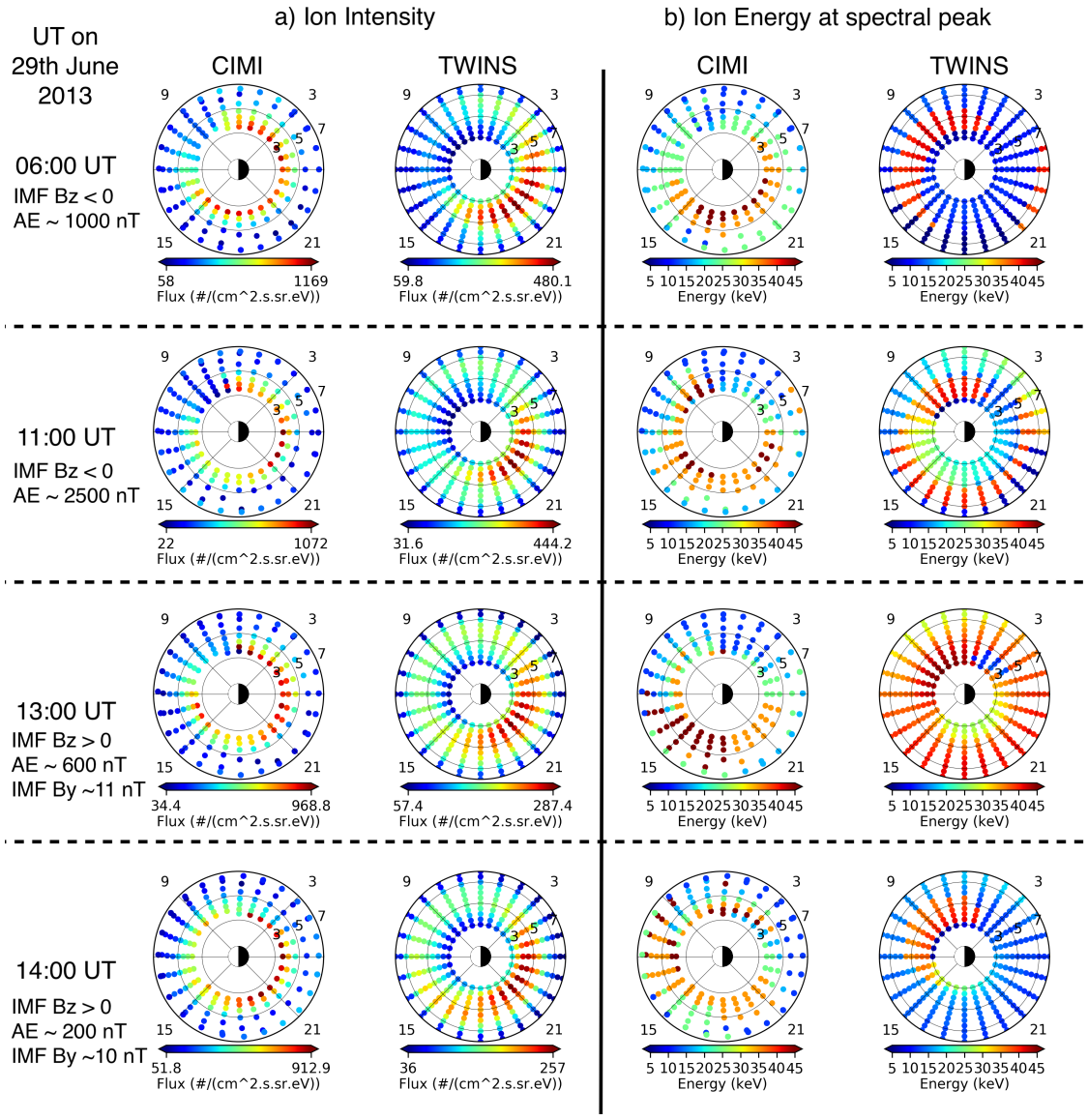

Figure 3. a. and b. show Equatorial spatial profiles of TWINS (right) and CIMI (left) ion intensity and median ion energy respectively at 06:00, 11:00, 13:00 and 14:00 UT on 29th June (top to bottom).The sun is located to the left and the azimuthal coordinates represent MLT. The radial coordinates represent the radial locations mapped to SM equator. The concentric radial circles mark radial locations of $2R_E$, $4R_E$ and $6R_E$ in CIMI.

prise of ions with peak energies at ∼35-45 keV whereas in TWINS it is ∼10-15 keV (Figure 3b top row). This could be due to the differences in the ion populations of two peaked energy spectra shown in Figure 2c (top row). At 11:00 UT (Figure 3a second row), the RC ions were more localized in MLT and were concentrated between MLTs of 18-3 hours in TWINS observations and 18-6 hours in CIMI simulations. In these MLT sectors the distributions of energies at peak of ion spectra shows that ion energies increase with location from morning-midnight-noon sectors in both CIMI and TWINS (Figure 3b second row). This is expected as the higher energy ions will drift faster and reach the noon sector before lower energy ions. Further, comparison of Figure 3a top row with second row shows that the RC was found to shift slightly radially inward from 06:00 UT in both CIMI and TWINS profiles.

At 13:00 UT (Figure 3a third row), the ion intensity distributions for CIMI and TWINS are mostly in agreement with each other with the bulk of the RC being located in the morning-midnight-dusk sectors. Another thing to note here is that compared to 11 UT (Figure 3a second row), the ring current intensity distributions have moved radially outward for both CIMI and TWINS at 13 UT. This indicates that inclusion of ion injections in CIMI simulations captures the effects of shielding electric fields better as in the study by Shekhar et al. (2021), this effect was not observed in CIMI. The distributions of ion energies at peak of ion spectra shown in Figure 3b third row show that where the bulk of the ring current ions are located, i.e. between 15-3 MLT, 3-5 R_E in TWINS and 13-6 MLT, 3.5-4.5 R_E in CIMI, the ion energies increase from 15-45 keV in CIMI and 15-35 keV in TWINS. At 14:00 UT (Figure 3a last row), the bulk of the ring current ions are located between 15-5 hours MLT sectors for both CIMI and TWINS. The spatial distibution of ion energies at peak ion spectra in Figure 3b last row are very different for CIMI and TWINS. This is likely due to TWINS ion spectra being two peaked compared to CIMI as shown in Figure 2c last row.

5.3 Comparisons with Shekhar et al. (2021)

The full evolution of TWINS and CIMI ion pressure peak locations (radial and azimuthal) are plotted in Figure 4a and b respectively. CIMI simulation results from Shekhar et al. (2021) (CIMI-old) are also plotted for comparison. Figure 4a shows that in general, CIMI ion pressure peaks are located radially inward compared to TWINS and show lesser fluctuations. Radial locations of CIMI ion pressure peaks from Shekhar et al. (2021) agree better with TWINS than the CIMI simulations performed in this study. This radial compresion is likely due to the fact that the outer boundary of CIMI simulations in Shekhar et al. (2021) was ∼10R_E whereas in this study it was ∼6.6R_E due to the locations of the LANL satellites. As such most distributions from the CIMI simulations performed in this study are radially compressed compared to CIMI-old.

The MLT locations of ion pressure peaks from CIMI-old, CIMI and TWINS are plotted in Figure 4b. From the onset of magnetospheric convection starting at noon on 28th June to the recovery phase of the storm starting at 06 UT on 29th June, both CIMI-old and CIMI produce ion pressure peaks located near midnight which are also mostly in agreement with TWINS. In the recovery phase and a couple of hours before, CIMI simulations incuding ion injections produce multiple ion pressure peaks which had not been observed in CIMI simulations performed by Shekhar et al. (2021).

6 Conclusions

In a recent study by Shekhar et al. (2021), a moderate geomagnetic storm (sym-H∼-100 nT) during 28th-29th June 2013 was examined using CIMI simulations results and global ring current observations from TWINS. However, the CIMI simulations (CIMI-old) did not include ion injections. We re-examined the same storm using CIMI simulations coupled with geosynchronous ion fluxes at 6.6R_E from 6 LANL satellites provid-

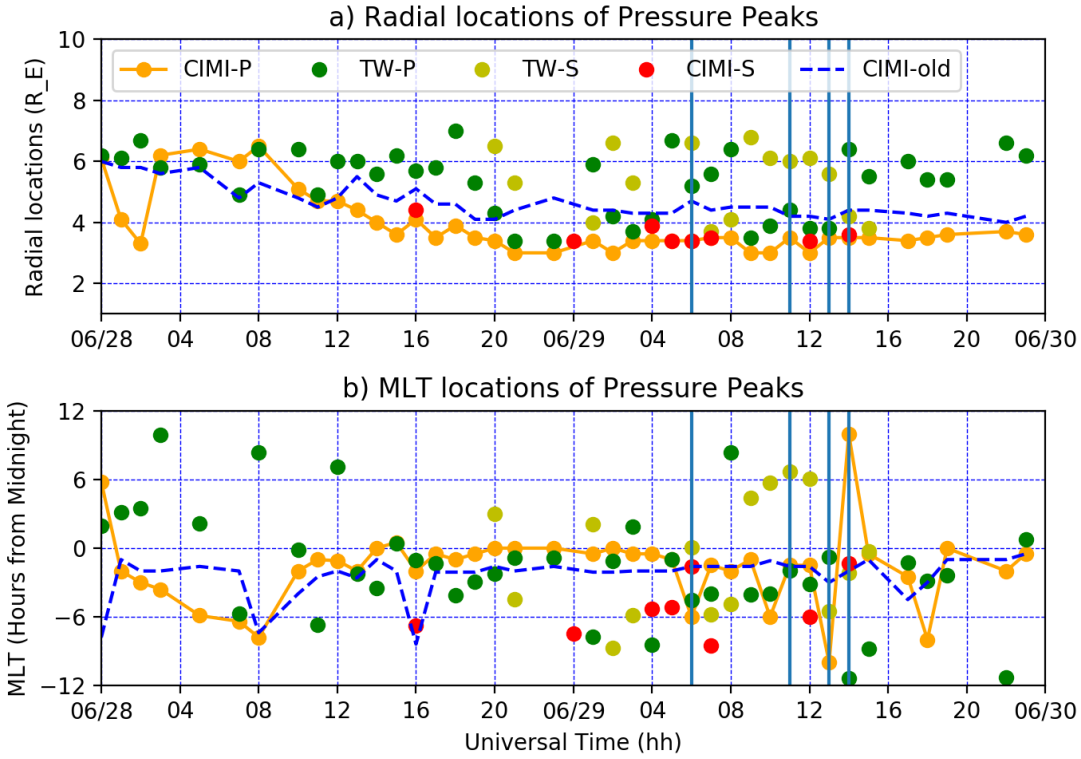

Figure 4. a: Radial locations of ion pressure peaks are plotted vs time from 00:00 UT on 06/28/2013 to 00:00 UT on 06/30/2013 for CIMI and TWINS. b: MLT locations of ion pressure peaks are plotted vs time from 00:00 UT on 06/28/2013 to 00:00 UT on 06/30/2013 for CIMI and TWINS. The times where detailed analysis are described in Section 5 are marked as blue vertical lines. TW-P/CIMI-P shows the locations of the largest ion pressure peak and TW-S/CIMI-S shows the locations of second largest ion pressure peak in TWINS data/ CIMI simulations. CIMI-old shows simulation results from Shekhar et al. (2021).

ing good MLT coverage, to account for ion injections. These new results were then compared with TWINS observations, including ion pressure, anisotropy, intensity and median energy, the ion spectrum at the ion pressure peak location. The locations of ion pressure peaks were also compared with the CIMI simulation results from Shekhar et al. (2021). Overall, CIMI produced distributions which were radially compressed relative to TWINS for all times during the storm. This is due to the fact that CIMI tends to overestimate the strength of convection at larger L shells and as a result, the penetration of particles. One possibility is that the background conductivity may be too low. Ion pressure and ion intensity profiles were an order of magnitude larger in CIMI compared to TWINS.

1. From the onset of magnetospheric convection starting at noon on 28th June to the recovery phase of the storm starting at 06 UT on 29th June, both CIMI-old and CIMI produce ion pressure peaks located near midnight which are also mostly in agreement with TWINS.
2. At the start of the recovery phase (06 UT on 29th June), the ion pressure distributions produced by CIMI showed two distinguishable ion pressure peaks at MLT locations in agreement with TWINS observations. Further, a double peaked ion energy spectrum was observed at the biggest ion pressure peak location for both CIMI and TWINS.
3. Between 11-13 UT IMF Bz turned northward after being constantly southward for $\sim$ 13 hours. The RC ion intensity profiles in both CIMI and TWINS were seen to shift radially outward at 13 UT compared to 11 UT. This indicates that both CIMI and TWINS may have observed effects of electric field shielding on the RC intensity distributions.
4. Between 13-14 UT, the ion intensity profile is seen to shift radially inward and slightly westward compared to 13 UT in TWINS observations. At this time IMF By was >5 nT, IMF Bz $\sim$-2 nT and v_{sw} $\sim$440 km/s. This indicates that shielding electric fields and/or twisting of the convection due to large IMF By (Weimer, 1995; Cson Brandt et al., 2002) may have led to the observed westward azimuthal shifts in proton intensities.

In several previous in–situ data and RC models, bulk of the RC pressure has been found to be concentrated in the dusk sector (Ebihara et al., 2002; Le et al., 2004; Jorgensen et al., 2004; Anderson et al., 2005; Shi et al., 2006; Perez et al., 2018; Shekhar et al., 2021). In our study, we found that including the effects of ion injections in CIMI simulations captured the shifts in the ion pressure peaks which were in agreement with TWINS global observations. Further, it also improved the model results for electric field shielding effects and TWINS and CIMI results were found to agree on the general features of the ring current. However, TWINS spatial profiles was more sensitive to fluctuations in the AE index compared to CIMI simulations. In future, it would be interesting to examine such comparisons for more geomagnetic storms so that global RC dynamics can be understood better.

Acknowledgments

This work was supported by the TWINS mission, a part of NASA'a Explorer Program. All simulations in this study were performed on the Auburn University High Performance and Parallel Computing Facility (https://hpc.auburn.edu/hpc/index.php).

Open Research

Data Availability Statement

The CIMI simulation data are available at https://doi.org/10.5281/zenodo.6611773. TWINS data for the geomagnetic storm studied in this paper are accessible from the Auburn University COSAM repository (https://www.auburn.edu/cosam/twins/cat_2/28-29-june-2013/). The OMNI solar wind data are available at omniweb.gsfc.nasa.gov.

References

Anderson, B. J., Ohtani, S. I., Korth, H., & Ukhorskiy, A. (2005). Storm time dawn-dusk asymmetry of the large-scale Birkeland currents. *Journal of Geophysical Research: Space Physics*. doi: 10.1029/2005JA011246

Cson Brandt, P., Ohtani, S., Mitchell, D. G., Fok, M.-C., Roelof, E. C., & Demajistre, R. (2002). Global ENA observations of the storm mainphase ring current: Implications for skewed electric fields in the inner magnetosphere. *Geophysical Research Letters*. doi: 10.1029/2002gl015160

Ebihara, Y., Ejiri, M., Nilsson, H., Sandahl, I., Milillo, A., Grande, M., ... Roeder, J. L. (2002). Statistical distribution of the storm-time proton ring current: POLAR measurements. *Geophysical Research Letters*. doi: 10.1029/2002GL015430

Fok, M. C., Buzulukova, N. Y., Chen, S. H., Glocer, A., Nagai, T., Valek, P., & Perez, J. D. (2014). The comprehensive inner magnetosphere-ionosphere model. *Journal of Geophysical Research: Space Physics*. doi: 10.1002/2014JA020239

Fok, M. C., Horne, R. B., Meredith, N. P., & Glauert, S. A. (2008). Radiation Belt Environment model: Application to space weather nowcasting. In *Journal of geophysical research: Space physics.* doi: 10.1029/2007JA012558

Fok, M. C., Moore, T. E., Wilson, G. R., Perez, J. D., Zhang, X. X., Son Brandt, P. C., ... Wolf, R. A. (2003). *Global ENA image simulations.* doi: 10.1023/B:SPAC.0000007514.56380.fd

Fok, M.-C., Wolf, R. A., Spiro, R. W., & Moore, T. E. (2001). Comprehensive computational model of Earth's ring current. *Journal of Geophysical Research: Space Physics*. doi: 10.1029/2000ja000235

Goldstein, J., & McComas, D. J. (2013). *Five years of stereo magnetospheric imaging by TWINS.* doi: 10.1007/s11214-013-0012-8

Hardy, D. A., Gussenhoven, M. S., Raistrick, R., & McNeil, W. J. (1987). Statistical and functional representations of the pattern of auroral energy flux, number flux, and conductivity. *Journal of Geophysical Research*. doi: 10.1029/ja092ia11p12275

Harel, M., Wolf, R. A., Reiff, P. H., Spiro, R. W., Burke, W. J., Rich, F. J., & Smiddy, M. (1981). Quantitative simulation of a magnetospheric substorm 1. Model logic and overview. *Journal of Geophysical Research*. doi: 10.1029/ja086ia04p02217

Heinemann, M. (1990). Representations of currents and magnetic fields in anisotropic magnetohydrostatic plasma. *Journal of Geophysical Research*. doi: 10.1029/ja095ia06p07789

Jorgensen, A. M., Spence, H. E., Hughes, W. J., & Singer, H. J. (2004). A statistical study of the global structure of the ring current. *Journal of Geophysical Research: Space Physics*. doi: 10.1029/2003JA010090

Le, G., Russell, C. T., & Takahashi, K. (2004). Morphology of the ring current derived from magnetic field observations. *Annales Geophysicae*. doi: 10.5194/angeo-22-1267-2004

McComas, D. J., Allegrini, F., Baldonado, J., Blake, B., Brandt, P. C., Burch, J., ... Zoennchen, J. (2009). The two wide-angle imaging neutral-atom spectrometers (TWINS) NASA mission-of-opportunity. *Space Science Reviews*. doi: 10.1007/s11214-008-9467-4

McComas, D. J., Buzulukova, N., Connors, M. G., Dayeh, M. A., Goldstein, J., Funsten, H. O., ... Valek, P. (2012). Two wide-angle imaging neutral-atom spectrometers and interstellar boundary explorer energetic neutral atom imaging of the 5 April 2010 substorm. *Journal of Geophysical Research: Space Physics*. doi: 10.1029/2011JA017273

Perez, J. D., Edmond, J., Hill, S., Xu, H., Buzulukova, N., Fok, M. C., ... Valek, P. (2018). Dynamics of a geomagnetic storm on 7-10 September 2015 as

observed by TWINS and simulated by CIMI. *Annales Geophysicae*. doi: 10.5194/angeo-36-1439-2018

Perez, J. D., Grimes, E. W., Goldstein, J., McComas, D. J., Valek, P., & Billor, N. (2012). Evolution of CIR storm on 22 July 2009. *Journal of Geophysical Research: Space Physics*. doi: 10.1029/2012JA017572

Shekhar, S., Perez, J. D., Davidson, K., & Fok, M. C. (2021). Comparison of CIMI Simulations and TWINS Observations on June 28 and 29, 2013. *Journal of Geophysical Research: Space Physics*. doi: 10.1029/2020JA028388

Shi, Y., Zesta, E., Lyons, L. R., Yumoto, K., & Kitamura, K. (2006). Statistical study of effect of solar wind dynamic pressure enhancements on dawn-to-dusk ring current asymmetry. *Journal of Geophysical Research: Space Physics*. doi: 10.1029/2005JA011532

Weimer, D. R. (1995). Models of high-latitude electric potentials derived with a least error fit of spherical harmonic coefficients. *Journal of Geophysical Research*. doi: 10.1029/95ja01755